The Influence of Tide and Wind on the Propagation of Fronts in a Shallow River Plume

Rijnsburger, Sabine; Flores, Raúl P.; Pietrzak, Julie D.; Horner-Devine, Alexander R.; Souza, Alejandro J.

DOI
10.1029/2017JC013422

Publication date
2018

Document Version
Final published version

Published in
Journal of Geophysical Research: Oceans

Citation (APA)
Rijnsburger, S., Flores, R. P., Pietrzak, J. D., Horner-Devine, A. R., & Souza, A. J. (2018). The Influence of Tide and Wind on the Propagation of Fronts in a Shallow River Plume. *Journal of Geophysical Research: Oceans*, *123*(8), 5426-5442. https://doi.org/10.1029/2017JC013422

Journal of Geophysical Research: Oceans

RESEARCH ARTICLE
10.1029/2017JC013422

The Influence of Tide and Wind on the Propagation of Fronts in a Shallow River Plume

Sabine Rijnsburger[1], Raúl P. Flores[2,3], Julie D. Pietrzak[1], Alexander R. Horner-Devine[2], and Alejandro J. Souza[4]

[1]Department of Hydraulic Engineering, Delft University of Technology, Delft, Netherlands, [2]Department of Civil and Environmental Engineering, University of Washington, Seattle, WA, USA, [3]Departamento de Obras Civiles, Universidad Tecnica Federico Santa Maria, Valparaiso, Chile, [4]CINVESTAV, Mérida, Mexico

Abstract In this study we used field data and radar images to investigate the influence of winds and tides on the propagation of tidal plume fronts. The measurements were collected in a shallow shelf region off the Dutch coast, 10 km north of the Rhine River mouth, and they clearly show the passage of distinct freshwater lenses and associated fronts at the surface that propagate all the way to the coastline. These fronts are observed as a sudden drop in near-surface salinity, accompanied by high cross-shore shear with onshore velocities at the surface. We determined the arrival time to our measurement site, frontal propagation speed, and structure of the fronts by combining the in situ data and radar images. Frontal Froude numbers show a wide range of values, with an average of 0.44. Our results show that fronts during spring tides are thinner, more mixed, and move faster relative to the ground during calm spring tides when compared to calm neap tides. Downwelling winds during spring tides result in thicker and faster fronts; however, the intrinsic frontal propagation speed indicates that the wind and tide control the frontal propagation mainly due to advection rather than by changing the frontal structure. Strong return currents in the near-bed layer resulting from fast and thick fronts increase near-bed turbulence and bed stresses. These high stresses suggest that the passage of fronts in shallow coastal areas can initiate sediment resuspension and contribute to transport processes.

Key Points:
- Differences in frontal properties are observed between calm spring and neap tides
- Downwelling winds lead to thick fronts, strong return currents, and high bed stresses
- The presence and propagation of a surface freshwater plume influence the stress and sediment stability at the bed

Correspondence to:
S. Rijnsburger,
s.rijnsburger@tudelft.nl

Citation:
Rijnsburger, S., Flores, R. P., Pietrzak, J. D., Horner-Devine, A. R., & Souza, A. J. (2018). The influence of tide and wind on the propagation of fronts in a shallow river plume. *Journal of Geophysical Research: Oceans*, *123*, 5426–5442. https://doi.org/10.1029/2017JC013422

Received 1 SEP 2017
Accepted 25 MAY 2018
Accepted article online 7 JUN 2018
Published online 10 AUG 2018

1. Introduction

River plumes are key in transporting freshwater, nutrients, contaminants, biota, and fine sediments into coastal areas (Dagg et al., 2004; Joordens et al., 2001; Kourafalou et al., 1996). They impact the ambient stratification and current structure and could have an impact on sediment transport in shallow areas. Understanding the processes impacting cross-shelf circulation and transport is valuable for areas that are vulnerable to sea level rise and coastal erosion (Kabat et al., 2009; Nicholls & Cazenave, 2010). The Dutch coast is a vulnerable coastal area dominated by the freshwater outflow of the Rhine and Meuse Rivers. The Rhine River flows into the shallow southern north sea, forming a 20- to 40-km-wide plume that extends 100 km along the Dutch coast (de Kok, 1996; de Kok et al., 2001; de Ruijter et al., 1992). Shallow frictional river plumes are also often referred to as regions of freshwater influence (ROFIs), which can be divided into three dynamical regions: the near-field, around the river mouth; the mid-field, where Earth's rotation starts dominating; and the far-field, where a buoyancy current flows parallel to the coast (Horner-Devine et al., 2015).

River plume fronts are sharp discontinuities in density at the boundary of the river plume, which are often visible at the surface as a line of foam resulting from horizontal convergence and downwelling (Garvine, 1974a). Strong fronts are often observed in the Rhine River plume as a result of river water discharged from the estuary on ebb tide. Discharged pulses of freshwater form freshwater lenses, which are advected by the tide, ultimately moving on top of the background plume before being mixed into it. At the edges of these lenses fronts are formed due to convergence with the ambient current. Using an idealized model both de Boer et al. (2008) and Fischer et al. (2009) observed the passage of a freshwater front 8–10 km north of the outflow area (around HW+2 hrs).

The fronts observed in the Rhine are similar to the tidal plume fronts observed in many river plume systems. Prior studies, such as Garvine and Monk (1974), found that tidal plume fronts in the near-field are dynamically

similar to nonrotating gravity current fronts described using experimental and theoretical gravity current models (Benjamin, 1968; Britter & Simpson, 1978). In reality tidal plume fronts are seldom two-dimensional as shown in the Connecticut River plume, where an ambient tidal flow normal to the direction of frontal propagation has been observed to cause asymmetric spreading of the plume (Garvine, 1974b; O'Donnell, 1988, 1990). They found that part of the front is hindered by the opposite directed tidal flow causing the front to thicken. Additionally, field studies have observed convergence and downwelling at the tip of tidal plume fronts with convergence rates of -0.01 to -0.09 s^{-1} and corresponding downwelling velocities of −0.03 to −0.20 m/s (Garvine & Monk, 1974; Marmorino & Trump, 2000; O'Donnell et al., 1998).

Prior studies have investigated the important influence of wind on plume dynamics and transport, showing that upwelling winds make the plume wider, thinner, and eventually detach it from the coast (Fong & Geyer, 2001), whereas downwelling winds compress the plume against the coast, causing the plume to narrow and thicken (Lentz & Largier, 2006; Moffat & Lentz, 2012). These wind-induced plume dynamics are also expected to impact the behavior of the plume fronts. Upwelling winds are expected to mix and weaken the offshore plume front, while downwelling winds may intensify fronts as a result of deepening.

The Rhine ROFI is not a classical surface-advected plume attached to the coast as defined by Yankovsky and Chapman (1997). In the southern North Sea the combination of significant tidal amplitudes and a shallow shelf result in a strongly frictional system. The tide propagates as a Kelvin wave along the Dutch coast and the combination of the tidal dynamics, high friction, vertical stratification due to the plume and Earth's rotation result in cross-shore tidal straining. Visser et al. (1994) found that during calm conditions (such as neap tide) tidal currents rotate anticyclonically near the surface and cyclonically near the bed, leading to counter rotating ellipses. This means that the direction of the tidal currents change at the surface and the bed during one semidiurnal tidal cycle, leading to cross-shore vertically sheared tidal currents that interact with the horizontal density gradient inducing and destroying vertical stratification during one tidal cycle. This process is called cross-shore straining or tidal straining and is dominant in the far field, 30–80 km downstream from the river mouth (de Boer et al., 2008; Rijnsburger et al., 2016; Simpson & Souza, 1995; Souza & Simpson, 1996). From low water (LW) to high water (HW) the cross-shore currents are directed offshore at the surface and onshore near the sea bed. As a result the plume is displaced offshore and due to continuity this leads to upwelling at the coast (de Boer et al., 2007) and an increase of vertical stratification. From LW to HW the cross-shore currents are directed onshore at the surface and offshore near the bed, advecting the plume back onshore. This leads to downwelling and mixing, resulting in a decrease of stratification. The entire Rhine ROFI, with freshwater lenses, is advected anticyclonically by the tidal currents during one tidal cycle.

Fine sediment transport is important for the Dutch coast, because of its vulnerability to coastal erosion and flooding. Therefore, limitations were set for the turbidity in the coastal region due to the construction of large scale engineering projects such as an extension of the Port of Rotterdam, and the Sand Engine (Stive et al., 2013). Prior studies have shown that Rhine plume fronts can carry fine suspended sediment offshore, due to the cross-shore velocity associated with their passage (Flores et al., 2017; Horner-devine et al., 2017). These studies showed that cross-shore sediment transport is dynamic and influenced by different processes, such as plume fronts, while alongshore transport based on resuspension or advection mainly is determined by the tide that moves back and forth along the coast. They did not explore the role of the fronts on the seabed, as was done for the Columbia River plume, where strong fronts were observed to impact the bottom boundary layer (Nash et al., 2009; Orton & Jay, 2005; Spahn et al., 2009).

The main objective of this study is to investigate the properties of the freshwater fronts, how wind and tide influence their propagation, and whether the tidal plume fronts impact the sea bed. To achieve this, we use in situ data taken 10 km north of the Rhine River mouth in the midfield plume, where we have two mooring sites as part of the STRAINS II field campaign (STRAtification Impacts Near-shore Sediment). First, we investigate the applicability of traditional gravity current theory (Benjamin, 1968; Britter & Simpson, 1978) on the propagation of freshwater fronts in the Rhine ROFI, where tidal advection and straining play an important role. We examine to what extent they are similar to the near-field tidal plume fronts found in other systems, such as the Connecticut or Columbia river plumes. Then we explore how the edges of the freshwater lenses are influenced by winds and spring-neap tides. Finally, we ask whether these fronts can have an impact on the sea bed.

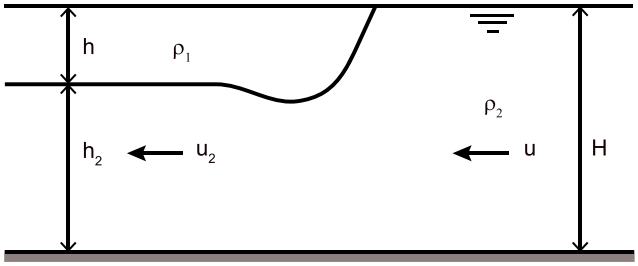

Figure 1. Schematic of an idealized gravity current in a front-following reference frame.

2. Gravity Current Theory

Many tidal plume fronts have been compared to gravity current theory (Garvine & Monk, 1974; Kilcher & Nash, 2010; Luketina & Imberger, 1987). A gravity current can be divided into two regions, the head region where mixing and large horizontal density gradients occur, and the tail where the current is stable (Britter & Simpson, 1978). Following Benjamin (1968), the theory describes the propagation of a gravity current moving with the front in a two-dimensional system. The front is stationary with respect to the ambient flow, the flow far upstream and downstream are assumed hydrostatic and mixing and friction are neglected. Figure 1 shows a schematic of a 2-D gravity current, where a surface current with a density of ρ_1 propagates into an ambient fluid with speed u. The ambient fluid has a density ρ_2 and a total depth H. The thickness of the surface current just after the head is defined as h, the thickness of the ambient flow there is h_2 with an assumed velocity of u_2. The ambient fluid should accelerate below the surface current based on continuity. Following the derivations, the return flow u_2 is a function of H/h_2 and u resulting in a larger u_2 for a larger h.

Benjamin (1968) defined the Froude number based on the reduced gravity and the relative thickness, h/H, where h is the current depth and H the total depth. The Froude number is predicted as $F_h = u/\sqrt{g'h} = \sqrt{2}$ for a current in a deep ambient fluid. The Froude number is dependent on the total water depth, $F_H = u/\sqrt{g'H}$, when h/H = 0.5 and gives a value of $F_H = 0.5$. He found a maximum value of $F_H = 0.527$ for $h/H = 0.347$, for larger h/H the Froude number decreases again. When dissipation is included, the maximum current speed coincides with maximum dissipation corresponding to $h/H = 0.347$. In addition, Britter and Simpson (1978) showed with experiments that the mixing at the head of the current increases the estimated Froude numbers of Benjamin (1968). They found a maximum value of $F_h = 2.25$ for $h/H < 0.1$.

3. Measurements

3.1. Location and Instrumentation

Field measurements were conducted from 17 September to 17 October 2014 (year days 259 to 290) off the Dutch coast, which captures two full spring-neap tidal cycles. Two moorings and three bottom frames were deployed 2 and 6 km offshore, corresponding to depths of about 12 and 18 m, located 10 km northeast of the mouth of the Rotterdam Waterway (see Figure 2). The moorings consisted of Seabird Microcat Conductivity Temperature Depth (CTD) instruments at different locations over the vertical. In total, nine CTD instruments were used with sampling frequencies ranging from 20 to 60 s. The CTD instruments at the 12 m site were mounted at −1, −3, −7, −8, and −10.5 m below the sea surface and at the 18 m site at −1, −2.5, −10, and −15 m.

At both locations the vertical current structure was measured using a four beam RDI Workhorse acoustic Doppler current profiler (ADCP), which was located at a bottom frame, with a frequency of 1200 kHz. The ADCP data have vertical bins of 0.25 m, and the N-E velocity component is rotated into an along- and cross-shore component, with a rotation angle of 42.5° from the North. Positive alongshore velocities are directed to the northeast, and positive cross-shore velocities are directed offshore. The collected CTD and ADCP data are averaged over 10 min, based on the bursts of the ADCP. Unfortunately, the ADCP at the 18 m site only lasted until day 281.

The near bottom current structure at the 12 m site was measured using three Sontek acoustic Doppler velocimetry (ADV) instruments, which were located at a third bottom frame at 0.25, 0.50, and 0.75 m above the seabed. They sampled with a frequency of 16 Hz during bursts of 10 min every 15 min. The raw ADV data is despiked using the method of Goring and Nikora (2002). After despiking, the data are averaged over 10 min

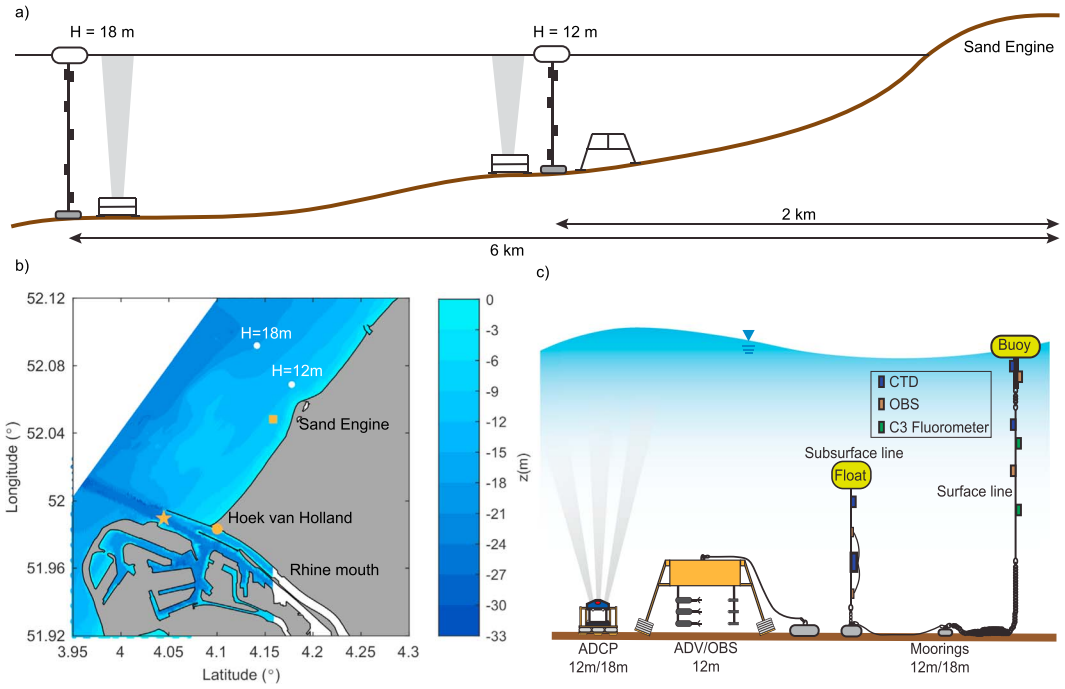

Figure 2. Study site and measurement setup. (a) Cross section of the measurement site, where at two locations a mooring and bottom frame are placed. The locations are at 12 and 18 m depth (about 2 and 6 km from the original coastline). (b) The Dutch coast around the Rhine River mouth. The figure shows the bottom topography (color), the Sand Engine, and the 2 measurement sites (white dots), about 2 and 6 km offshore, which are 10 km northeast of the river outflow. The orange square represents the measurement station for the wave data. The orange circle represents a meteorological measurement station, and the star represents the location for discharge data. (c) Detailed schematic of the measurement setup (Figure after Flores et al., 2017). A third frame is placed at 12 m depth.

giving a mean velocity. Turbulent velocity components (u', v', and w') were obtained by removing the 10-min averaged velocities. The N-E velocities are rotated into an along- and cross-shore component, in the same way as done for the ADCP instruments. The ADV instruments are located close to the seabed, where waves can influence the Reynolds stresses ($u'w'$, $v'w'$). The method of Shaw and Trowbridge (2001) is used to calculate the Reynolds stresses eliminating the influence of waves. This method requires two ADV instruments separated at a distance larger than the length scale of turbulent eddies, but smaller than the correlation scale of waves. For this calculation we used the lowest and highest ADV with a vertical distance of 0.5 m. This distance seems to be sufficient based on a comparison between the signal with and without wave removal. Additionally, the spectral density for the horizontal velocity component shows good agreement with the −5/3 slope characteristic of the inertial subrange (Flores et al., 2017).

X-band radar images from SeaDarQ are available with a field of view spanning the 12 m site and closer to shore. The raw data are averaged every 5 min resulting in time-averaged images. These images show tidal plume fronts propagating all the way to the coast, from which information such as frontal propagation speed (relative to the ground), the direction of propagation (respect to the coast), the exact location of the front in real world-coordinates, and the timing of frontal propagation through our mooring site can be extracted.

3.2. Estimation of Frontal Properties

The thickness of a front (h) is estimated using the cross-shore velocity profile. At the mooring sites when the front arrives, the thickness of the onshore velocity layer is estimated by taking the distance between the sea surface elevation and the point where onshore velocities turn into offshore velocities. Figures 5c and 5d show this calculation procedure, where 1-min averaged cross-shore velocity profiles are compared with the 10 min averaged velocity profile. This method gives a good estimate of the bulk thickness of the stratified water mass for most of the fronts. It does not always give an accurate thickness of the head of the front. For some fronts the thickness might be underestimated with this method (Figures 5a and 5c), which could have a small effect on our analyses.

We set up a front tracking procedure to calculate the intrinsic frontal speed U_f using the radar images (see Appendix A for more details). The radar images are used to determine the orientation of the front and the frontal speed relative to the ground (u_f). The intrinsic frontal speed is defined relative to the motion of the ambient current in a front-normal system, $U_f = u_f - u_a$, where u_f is the total velocity at the timing of the front relative to the ground (Benjamin, 1968; Garvine & Monk, 1974). The ADCP data and the orientation of the front are used to determine the front normal ambient velocity (u_a). The frontal speed is used to calculate the Froude number, $F_H = U_f / \sqrt{\frac{\rho_2 - \rho_1}{\rho_2} gH}$, where ρ_1 is upper layer density, ρ_2 the lower layer density, H the water depth. The definition of the Froude number for large h/H has been chosen (Benjamin, 1968; Shin et al., 2004). A quality check of the radar images resulted in a limited number of images that could be used, resulting in a total of 17 frontal speeds and Froude numbers.

Bottom stresses are determined as $\tau_b = \rho(\overline{u'w'}^2 + \overline{v'w'}^2)^{1/2}$, where ρ is the density of the salter bottom water. The stresses are rotated into an along-front and across-front direction as explained above. In addition, the vertical fluctuation w' obtained from the ADVs is used to determine the TKE dissipation rate (ϵ) by fitting spectra to the inertial subrange (e.g., Voulgaris & Trowbridge, 1998).

3.3. Environmental Conditions

The environmental conditions were highly variable during the entire measurement period (Figure 3). Wind speed and direction were measured by the Royal Dutch Meteorological Office (KNMI) at a station near Hoek van Holland (Figure 2). These wind speeds have been used to estimate the alongshore wind stress using a quadratic drag law with a drag coefficient C_{10} of 0.001 and air density of 1 kg/m^3 (De Boer et al., 2006). Positive alongshore wind stress is directed to the northeast. The beginning of the field campaign coincided with neap tide and winds lower than 5 m/s (Figures 3a–3c). During this period, strong stratification was observed, reaching a maximum top-bottom salinity difference of 8 psu and a mean of 3.5 psu (Figure 3f). Northerly winds (360°) with a maximum of about 15 m/s were present during the first storm from days 264 to 266. During this storm event no stratification was observed (Figure 3f), as upwelling winds mixed the plume and displaced it southward and offshore from the moorings. After the storm, wind speed ranged between 3 and 9 m/s with variable wind direction from days 266 to 280. The relaxation of the wind resulted in an onset of stratification after day 266. The maximum top-bottom salinity difference was 7.5 psu for spring tide and 8 psu for neap tide (Figure 3f). The second storm reached wind speeds of about 12 m/s coming from the south (180°–200°) on days 280 to 284. Figure 3f shows the presence of low stratification during this storm event, which is the result of a downwelling wind.

Wave data were retrieved from a Waverider buoy 1 km southwest of the 12 m measurement site. High significant wave heights were aligned with high wind intensities, with a maximum significant wave height of 2.5 m during the first storm and 1.5 m during the second storm (Figure 3d). During calm conditions significant wave heights below 1 m were observed. The presence of waves during our field campaign led to the need of filtering the Reynolds stresses.

The discharge data of the Rhine and Meuse River are obtained from the database of Rijkswaterstaat (2015), where the discharges are extrapolated from data measured at Lobith, about 170 km upstream of the River mouth. Figure 3e shows the total discharge of both rivers, with a minimum of approximately 500 m^3/s, a maximum of about 2,500 m^3/s and a mean value of 1,600 m^3/s.

4. Results

4.1. Observations

Figure 4 shows the time series of salinity, alongshore velocity, cross-shore velocity and bottom stresses at the 12 m site, for two contrasting periods that were selected to analyze the variability in stratification and the impact of fronts. We chose a neap tide with low winds as a low energy reference period and a spring tide with moderate winds as a high-energy period (see Figure 3), where the moderate winds were not strong enough to mix out the front. Figures 4a–4e shows results from the first 2 days of the measurement campaign during neap tide with winds below 5 m/s (between days 260 and 263). Figures 4f–4j shows results from 2 days during spring tide with 7–10 m/s winds mainly coming from southwest (SW; days 268 to 270). In both subfigures a X-band radar image is shown for the corresponding neap and spring time series.

A sudden decrease in surface salinity was observed at day 260.4 during neap tide (Figure 4b), about 2 hr after high water (HW+2). At the same moment a strong cross-shore shear develops, where the surface current

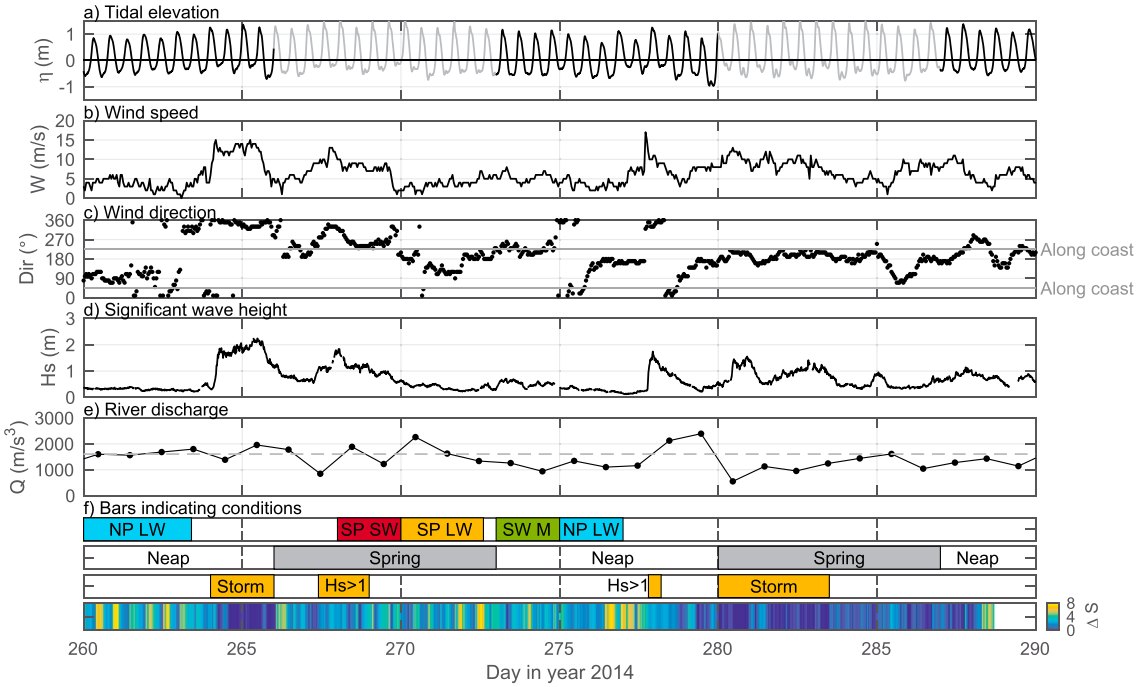

Figure 3. The conditions during the measurement campaign. (a) The tidal elevation at Hoek van Holland, 10 km southwest of the measurement site (black is neap, grey is spring). (b) The wind speed measured at Hoek van Holland and (c) the wind direction measured at Hoek van Holland. The grey lines indicate the direction of the coast (42.5° from the north) where the wind will be alongshore directed. (d) Significant wave height at wave rider buoy and (e) total river discharge from New Waterway and Haringvliet sluices, where the dashed grey line indicates the mean discharge of 1,600 m^3/s. (f) Bars indicate different periods based on tide and wind, spring/neap, the presence of storms and when $Hs > 1$, and vertical stratification in terms of salinity difference between bottom and surface (based on 12 m site).

is directed onshore and the bottom current offshore (Figure 4d). Every tidal cycle the same pattern is visible. This sudden decrease in salinity is due to a front passing by the measurement site as confirmed by the X-band radar image from the same period (Figure 4a). The front travels onshore causing an offshore return flow near the bottom (Horner-devine et al., 2017). This passage of fronts is also observed during the spring tide period (Figures 4f and 4g); however, the fronts arrive around HW at the 12 m site.

Figure 4 shows a difference in the salinity and cross-shore velocity structure between the two periods. The cross-shore shear is higher during the windy spring period than during the calm neap period, with values of 0.8 m/s at day 269.1 and 0.3 m/s at day 260.4, respectively. The bottom and surface cross-shore currents reverse around the same time. The flow reversal for the calm neap period is different, close to the bottom the flow reverses first slowly followed by the layers above. This results in a three-layer density system for the calm neap period and a two-layer system for the windy spring period. This is reflected in the salinity data as well, where Figure 4b shows a fresh upper layer, a medium middle layer and a saline lower layer. Figure 4g shows a thick fresh upper layer and a saline lower layer, which looks like a two-layer system. The upper layer is more mixed in this case, due to more tidal and wind energy.

The radar images show that the front slows down and turns as it propagates towards the coast. At the 12 m site the front propagates under an angle of about 30° – 40° with the coast, turning to become more parallel to the coast as it propagates onshore (Figures 4a and 4f). During the calm neap period the front is at the 12 m site at 09:52. It takes 2 hr and 15 min to reach the onshore position at 12:07 (Figure 4a). During the windy spring period the front needs 50 min to propagate from the 12 m site starting at 02:42 to the onshore position at 3:32 (Figure 4f). Therefore, the front during the calm neap period propagates much slower towards the coast than the front during the windy spring period.

An increase in bed stress is observed around HW and LW for both periods (Figures 4e and 4j, black line). This response coincides with the estimated tidal shear stress (red line). The tidal shear stress is estimated using a quadratic drag law, where the tidal velocity is obtained through harmonic analysis using a near-bottom averaged velocity and the T-Tide package (Pawlowicz et al., 2002). A drag coefficient C_D of about 0.0035 was

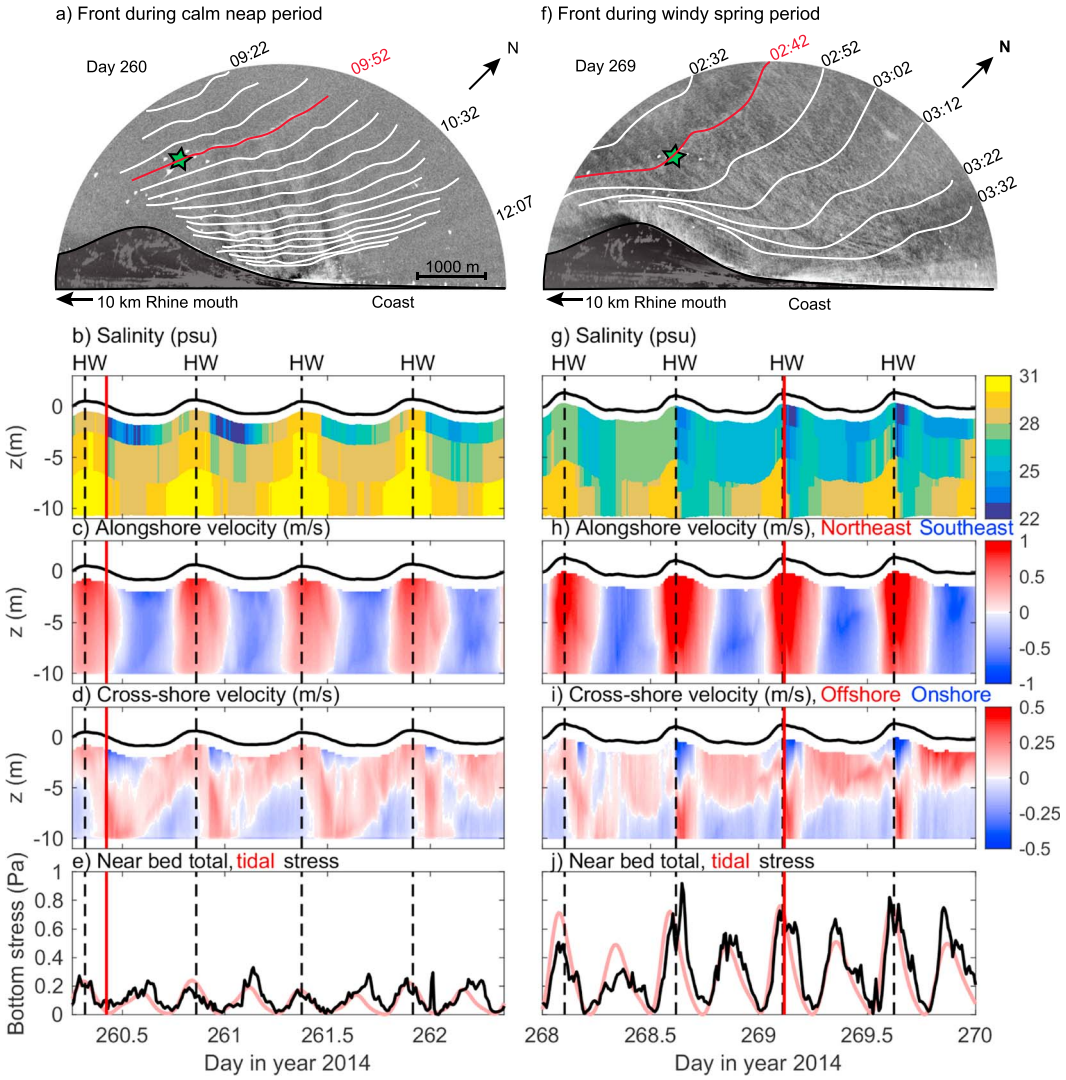

Figure 4. Radar images and time series of salinity (psu), alongshore velocity (m/s), cross-shore velocity (m/s), and bed stresses at the 12 m site. Panels (a) and (f) are X-band radar images with the trajectory of a front propagating towards the coast on day 260 and 269, where the green star represents the 12 m measurement site. The white lines have a time step of 10 min. The red line corresponds to the red line in the lower panels, indicating frontal passage. The left panels (b–e) represent the first 2 days of the first Neap period with winds lower than 5 m/s. The panels show time series of (b) salinity (psu), (c) alongshore velocity (m/s) where positive is northeastward, (d) cross-shore velocity (m/s) where positive is offshore. The vertical axis represents the depth and the horizontal axis the time in days of year. (e) Total stress 0.25 m above the bottom (Pa) averaged over 10 min (black line). The red line is the estimated tidal stress near the sea bed (Pa). The dashed black lines correspond to high water (HW). The right panels (g–j) represent 2 days during spring with moderate southwest wind.

found based on the measured wave-filtered Reynolds stresses and averaged bottom velocity. A second peak in the bed stress is observed just after HW during the spring tide period with moderate SW winds, which is just after the front passes through the mooring site (Figure 4j). This peak is not observed in the tidal stress. Therefore, the difference between the total bed stress and the estimated tidal stress indicates that besides the tide other processes increase the bed stress, such as the passage of the freshwater lens. For the calm neap period no second peak has been observed just after frontal arrival, the stress is mainly tidal driven.

The acoustic backscatter of the ADCP is used to get insight into the frontal structure (Figures 5a and 5b). Figure 5 shows 4.5 min of the structure of a calm neap front (a) and a windy spring front (b). The dashed line corresponds to the thickness inferred using the cross-velocities and seems to give a good approximation. The neap front shows first a raised head, followed by a minimum in thickness and then it increases

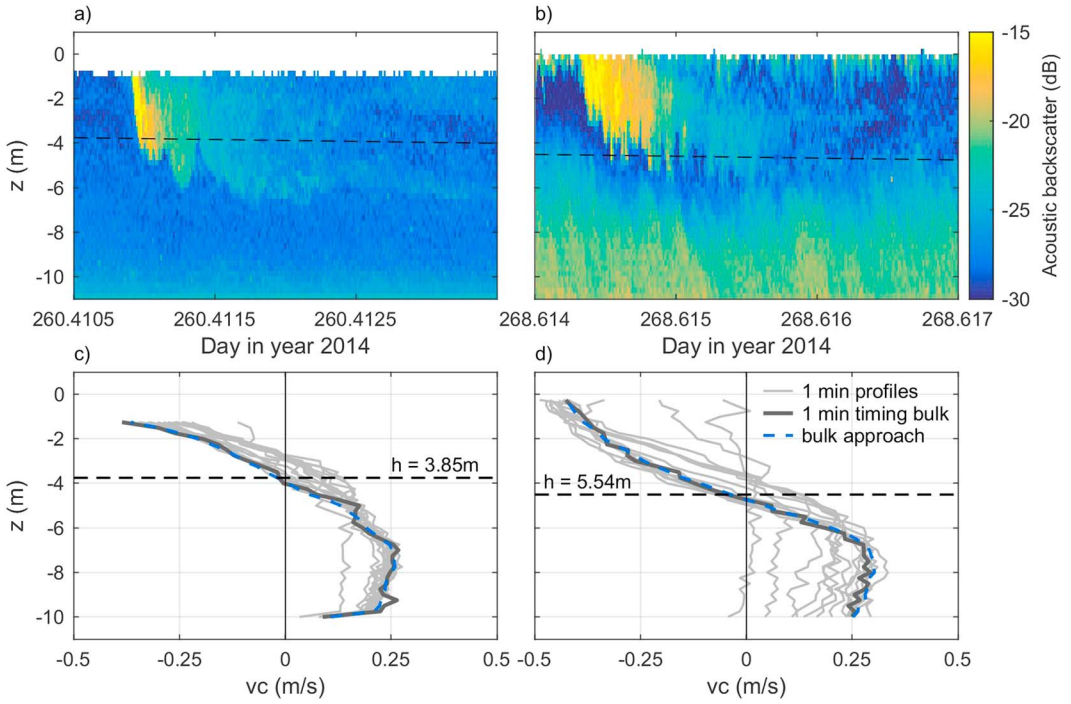

Figure 5. (a, b) Acoustic backscatter (dB) around frontal head. The horizontal axes show a time series of about 4.5 min, the vertical axes represents the depth. Horizontal dashed line is the estimated thickness of the plume based on cross-shore velocity. (a) Neap tide front, (b) Spring tide front with moderate Southwest wind. (c, d) Cross-shore velocity profile over the depth, where the dashed blue line is the 10-min averaged data used, light grey lines are profiles of 1-min averaged cross-shore velocity before the front arrives, dark grey line is the timing of the front for the 1-min averaged velocity data. (c) Neap tide front and (d) spring tide front with moderate Southwest wind.

to a constant thickness (Figure 5a). This structure is similar to the shape of gravity currents observed in the laboratory (Britter & Simpson, 1978; Shin et al., 2004). The spring front shows a slightly different structure, it does not show a clear raised head. The edge of the front seems to be less thick than the body behind it. A high backscatter signal near the seabed is observed during energetic periods (Figure 5b), which makes the distinction between stratification and sediment more difficult.

4.2. Tide and Wind Forcing on Frontal Dynamics

Figure 4 showed that the system behaves differently under different forcing conditions. In this section we investigate in more detail the influence of tide and wind forcing on the fronts. We look to the median properties of frontal thickness (h), reduced gravity (g'), and frontal arrival time to our 12 m mooring site relative to HW for different periods. Based on the entire time series we selected a few periods to investigate the influence of wind and tide: Neap tide with low winds (NP LW, light blue), Spring tide with low winds (SP LW, yellow), transition between Neap and Spring tide with SW winds between 4–7 m/s (SP-NP SW M, green), Spring tide with SW winds between 7–9 m/s (SP SW H, red; see Figure 3f for the corresponding days). Low winds are defined here as wind speeds smaller than 5 m/s. These abbreviations are used throughout the manuscript. Unfortunately, no radar images are available from the SP LW period.

4.2.1. Spring-Neap Variability

The neap and spring periods with low winds are used to identify the spring-neap variability for the frontal properties. For NP LW we expect the fronts to arrive around HW+2 based on previous research (De Boer et al., 2006, 2008; Simpson & Souza, 1995), which is inline with onshore advection and straining due to the tide. Figures 4b and 6c (blue) show indeed that the fronts on average arrive around HW+2. For SP LW the fronts arrive around 1 hr and 20 min after HW, which is earlier than on NP LW (Figure 6c, yellow). The earlier arrival on a spring tide is in agreement with the higher along- and cross-shore advection and straining (De Boer et al., 2006, 2008).

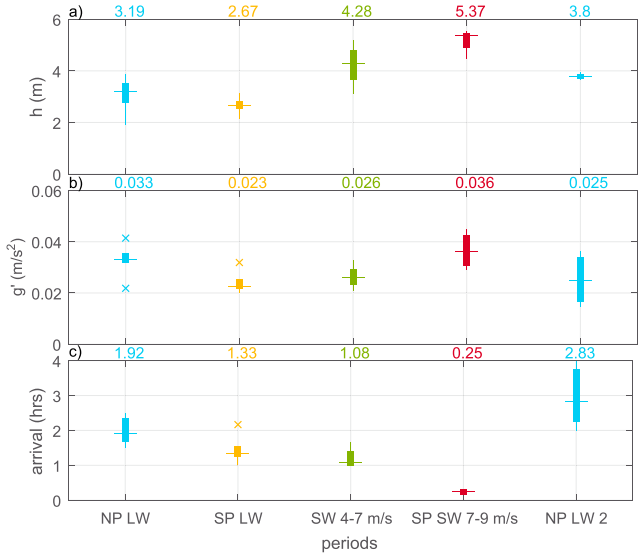

Figure 6. Boxplot of (a) frontal thickness (h), (b) reduced gravity (g'), and (c) arrival time relative to HW. On the horizontal axis different periods are displayed: Neap tide and low winds (blue), Spring tide and low winds (yellow), Spring-Neap 4–7 m/s SW winds (green), Spring 7-9 m/s SW winds (red), and another Neap tide with low winds (blue). The horizontal line is the median, the outliers are marked by a x, and the variability of the data is shown by the length of the box. The median is also written above each panel per period.

The larger advection and straining during spring tide is also visible in the upper layer velocity ($U_{1,adcp}$) as a function of tidal amplitude, where SP LW corresponds to larger velocities than NP LW (Figure 7b). These velocities and the arrival times include the effect of wind and tide; however, it does not reflect whether the intrinsic frontal speed is influenced by the tide. The frontal propagation speed shows a different result than the net velocity (Figure 7a), with a maximum speed of 0.55 m/s and a minimum speed of almost zero indicating an arrested front. A large tidal amplitude does not necessarily correspond to a front with high intrinsic frontal speed. Thus, Figure 7a suggests that tidal amplitude does not determine frontal propagation.

Figure 6 shows that neap fronts are thicker and more stratified than spring fronts under low wind conditions, suggesting that the spring fronts are more mixed. The lower g' on the spring tide reflects the stronger mixing expected during this period. So neap fronts are thicker and more stratified than spring fronts. A stronger or weaker tidal flow impacts the advection velocity of the fronts, whereas it does not seem to determine the intrinsic frontal speed.

4.2.2. Wind Variability

Figure 8 shows the relationship between the wind direction, wind speed, and the arrival time of the fronts relative to HW and the relative thickness of the fronts (h/H) for both mooring sites. The data are plotted in the form of a wind rose including the direction of the coast. The instruments for the 18 m site only measured for 28 days; therefore, fewer frontal points are shown in Figure 8a than in Figure 8b. A mean wind speed and direction averaged over 6 hr are used, to take the influence of the wind on the fronts beforehand into account as well.

Figures 8a and 8b indicates that winds from 195° to 270° correlate with the early arrival of a front associated with a fast propagation speed relative to the ground (HW+<1 hr). This can be explained using the frictional and Ekman component of the winds compared to the direction of the frontal propagation. The frictional component displaces the plume northeastward along the coast in case of a southwesterly wind (225°, alongshore). The Ekman component advects the plume and lenses within it towards the coast. The resulting wind velocity accelerates the front resulting in a higher speed. Figures 8c and 8d show larger h/H for the fronts related to winds coming from 195° to 270°. Winds from these directions are downwelling winds along the Dutch coast (from SW).

In contrast, wind directions between 0° and 195° result mainly in a later arrival of the front (HW+>1–1.5 hr), which can be explained as follows. Northeasterly winds (45°, alongshore) advect the front offshore (Ekman) and southwards (frictional), therefore the propagation of the front will be decelerated by the wind resulting

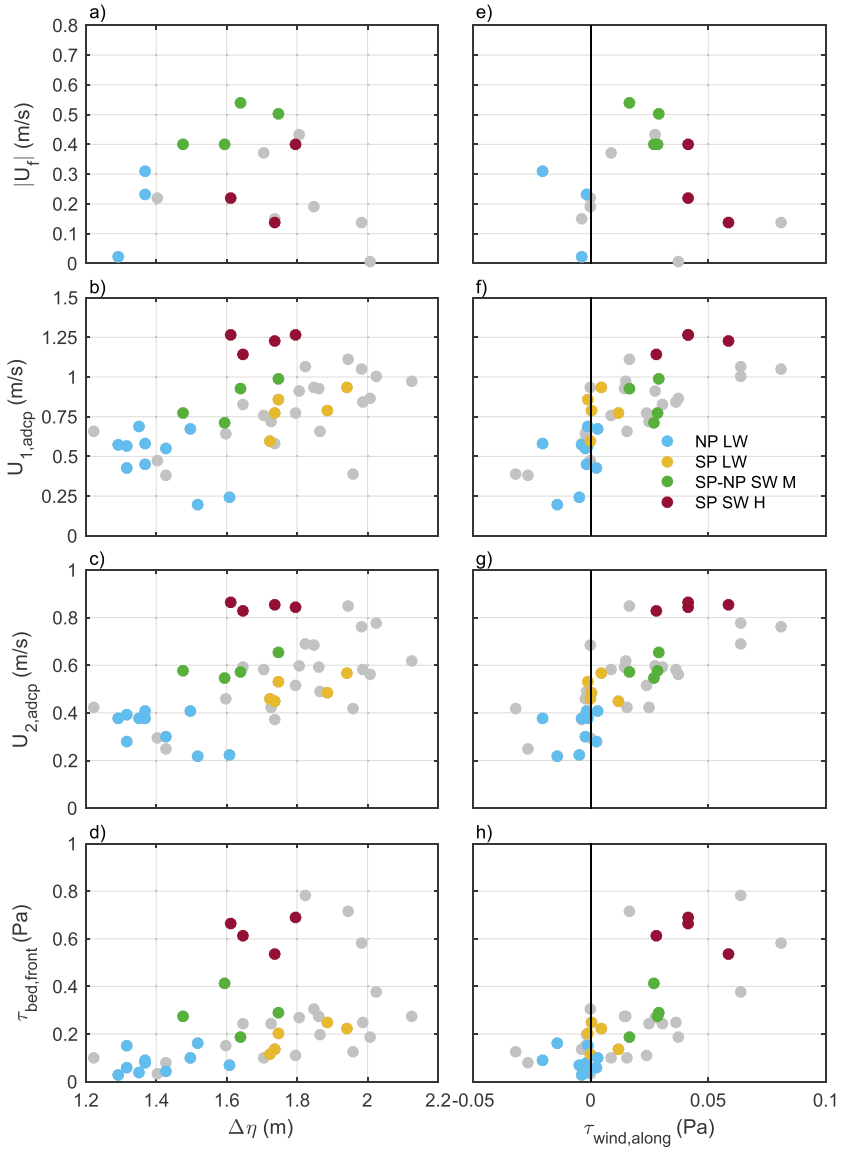

Figure 7. Tidal amplitude ($\Delta\eta$ in m) and alongshore wind stress ($\tau_{wind,along}$ in Pa). (a, e) Absolute intrinsic frontal speed, U_f (m/s). (b, f) Upper layer velocity at timing front relative to ground, $U_{1,adcp}$ (m/s). (c, g) Lower layer velocity at timing front relative to ground, $U_{2,adcp}$ (m/s). (d, h) Bed stress at timing front, $\tau_{bed,front}$ (Pa). Colors are related to different selected periods based on tide and wind, where blue is NP LW, yellow is SP LW, green is SP-NP SW M, and red is SP SW H.

in a lower propagation speed. An easterly wind (125°, offshore) should advect the plume and lenses offshore (frictional) and northeastward (Ekman), which should decelerate the fronts relative to a situation without winds. Figures 8c–8d show that these winds on average correspond to thinner fronts (small h/H).

When we look to median properties for different periods, a distinct difference between low and high winds have been observed (Figure 6). The fronts during periods with SW winds are thicker and arrive earlier than the neap and spring periods with low winds. The fronts during spring tide with high SW winds are the thickest and fastest, and these fronts are highly stratified as well. Based on gravity current theory, we would expect that thick fronts with a large density difference have higher intrinsic frontal speeds. Figure 7e shows that these fronts (red) do not necessarily show a high intrinsic speed (U_f), but they show a large upper layer velocity relative to the ground ($U_{1,adcp}$). A larger positive alongshore wind stress corresponds to a higher upper layer velocity, but not necessarily to a higher frontal speed. The transition period between neap-spring with medium SW winds correspond to high U_f and with less scatter than for the NP LW and SP SW H periods.

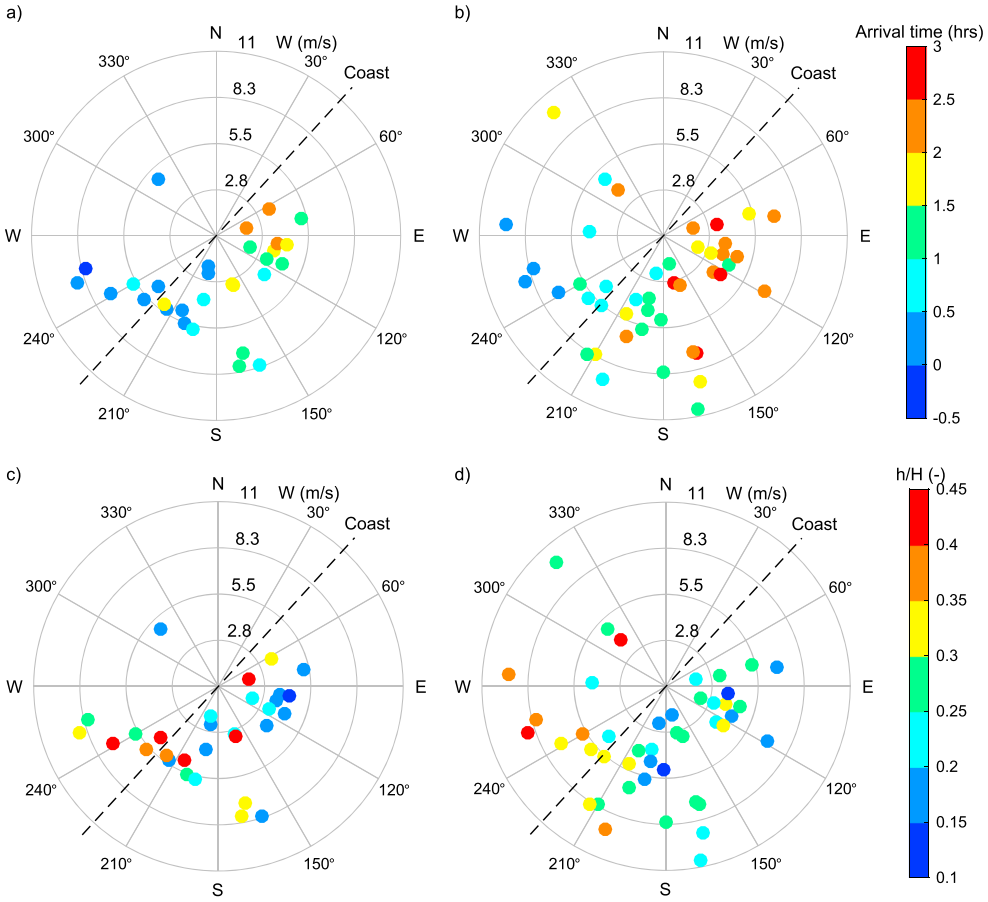

Figure 8. Wind rose diagram based on wind direction (following the circles) and wind speed. The dots represent the fronts, where the colors indicate arrival time (a–b) and relative thickness (c–d). (a) The arrival time relative to HW (hr) at the 18 m site and (b) the arrival time relative to HW (hr) at the 12m site. (c) Relative thickness h/H at the 12 m site. (d) Relative thickness h/H at the 18 m site. The dashed line indicates the direction of the coastline (42.5° from North).

4.3. Bed Stress

The observed differences in frontal dynamics under different tidal and wind forcing conditions suggest that we may also observe corresponding changes in bed stress resulting from frontal processes. Figure 4 showed a different behavior in the bed stress around frontal arrival during two different periods. During neap tide with low winds the bed stress is mainly tidal, but during spring tide with high SW winds an extra peak seems to be present. Figures 7d and 7h investigate whether there is a relation between the signal of the bed stress and the tide and wind at the time of the fronts. Figure 7 shows clearly a tidal signal in the bed stresses, where higher tidal amplitudes have a slightly higher bed stress relative to low tidal amplitudes. A maximum bed stress of 0.3–0.4 Pa has been observed, which is related to a tidal amplitude larger than 2 m, which seems to be mainly driven by the tide. However, there are some data points that behave differently. These data points correspond to higher bed stresses for different tidal amplitudes, suggesting that other processes also contribute.

Figure 7h shows good agreement between alongshore wind stress and bed stress at the time of the frontal passage. A positive wind stress is related to the downwelling component of the wind. So, large downwelling winds correspond to an increase in bed stress below the front. Large downwelling winds also relate to large upper and lower layer velocities (Figure 7), however, not necessarily to larger frontal speeds. Figures 6 and 8 showed that the fronts under forcing of SW winds are often thick. This should indicate that the increase in bed stress is observed under thicker fronts, which is confirmed by Figure 9b. So high bed stresses are linked to thick fronts under forcing of SW winds.

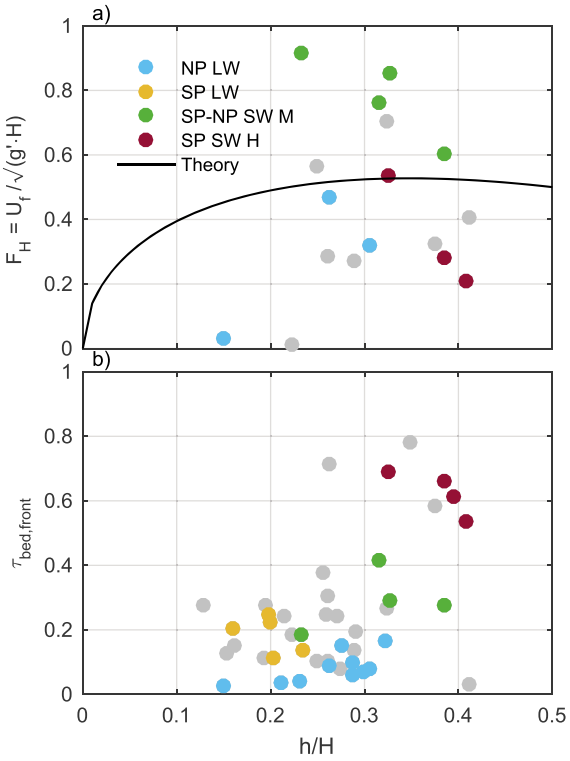

Figure 9. Relative thickness of fronts (h/H) versus (a) Froude number based on water depth (F_H) and (b) bed stress (Pa) at timing front ($\tau_{bed,front}$). The colors relate to the selected periods based on wind and tide. The black curve in (a) is the theoretical value based on Benjamin (1968).

5. Discussion

5.1. Comparison to Theory and Prior Laboratory and Field Results

Benjamin (1968) found a Froude number of 0.5 for a gravity current that reaches about half depth. Figure 9a shows his theoretical curve for the Froude number as a function of relative thickness. For the Rhine plume fronts the average Froude number was 0.44; however, the observed values ranged from 0.01 to 0.9 revealing a high degree of scatter around the theoretical value. One of the reasons could be the assumptions and estimates necessary for calculating the frontal speed (U_f), which could lead to some inaccuracy.

Estimates of frontal Froude number are challenging in the field due to the complexity of defining key quantities in three-dimensional irregular fronts. However, there are several physical processes that may also contribute to the scatter observed in the Froude number. One reason could be the location of our mooring site, for example, which is in the midfield plume instead of near-field. This location means that the front already traveled 10 km along the coast, which we expect to be around 8–12 hr after release. Therefore, we expect that the fronts already lost most of their energy and are influenced by earth rotation. This is different than most tidal plume front studies, where the fronts are studied in the near-field just after release (Kilcher & Nash, 2010). Some simple nonhydrostatic numerical simulations, using the model of Lamb (1994), with and without earth rotation indicate that the addition of Coriolis will slow the transit time of the fronts by about an hour. Additionally, our mooring site is located in a system dominated by tidal advection and straining as result of friction and rotation. These tidal processes are key in determining the location and movement of the entire plume and lenses within it as shown by, de Ruijter et al. (1997), Van Alphen et al. (1988), Simpson and Souza (1995) and de Boer et al. (2008).

The relative thickness of the fronts in the Rhine plume is large compared to other tidal plume systems (Garvine & Monk, 1974; Horner-Devine et al., 2013; Kilcher & Nash, 2010; Luketina & Imberger, 1987, e.g.). In these systems values for h/H are often in the range of 0.04 to 0.12, while we found values in the range of 0.13 to 0.41. For systems with thin fronts, Froude number in terms of the current depth is used, $F_h = U_f/\sqrt{gh}$ where they found values in the range of 1 to 2.7. Mean frontal velocities of 0.7-0.8 m/s are found for the Columbia plume

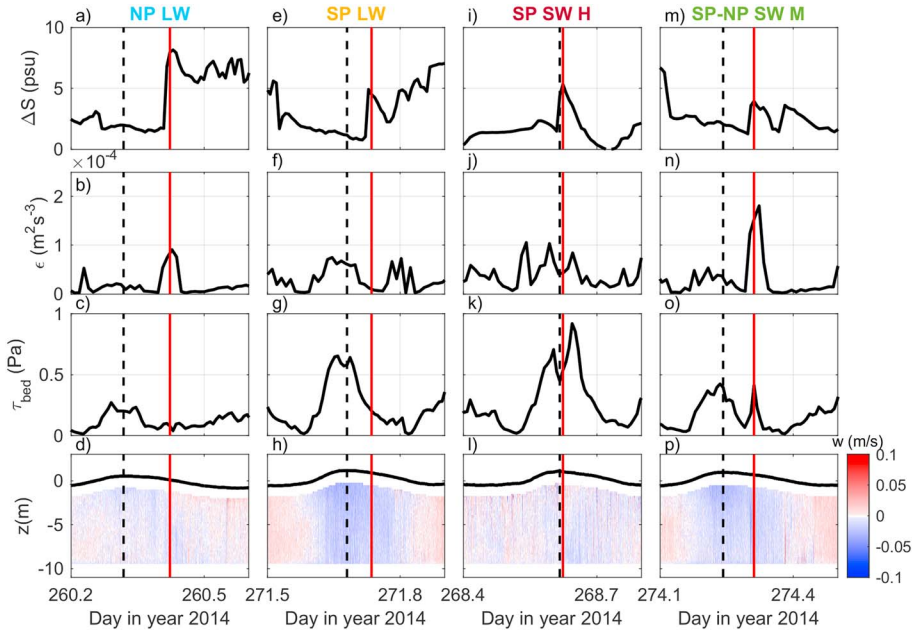

Figure 10. Near bed properties for different periods. The vertical axes represents salinity difference bottom-top (psu), dissipation (m^2/s^3), bed stress (Pa), and depth (m). The horizontal axes represent different periods: NP LW, SP LW, SP SW H, and SP-NP SW M. The colorbar in the fourth row represents vertical velocity (m/s) based on 1-min averaged ADCP data, where positive is upwards and negative downwards. The dashed black lines indicate HW and the solid red lines indicate the front.

(Nash & Moum, 2005; Orton & Jay, 2005), while for the Merrimack a value of 0.39 m/s have been observed (Horner-Devine et al., 2013). The frontal velocities we found are in the range of 0 to 0.54 m/s, which is in the same range as the values found in other plume systems. Our system is influenced by a strong tidal flow similar as observed by Garvine and Monk (1974) in the Connecticut. Near the mouth the spreading of the lenses should be asymmetrical as well due to the tidal background flow.

5.2. Impact of Wind and Tide on Frontal Structure

We observe that downwelling winds accelerate the fronts, presumably by advecting the front towards and along the coast, consistent with Ekman wind driven transport. However, at 10 km downstream we find Rossby numbers in the range of 0.2 to 0.5 based on a velocity of 1.2 m/s and a length scale in the range of 20 to 40 km (de Kok, 1997). de Kok (1997) stated that the plume is in semi-geostrophic balance 15 km downstream. In classic geostrophic downwelling theory a thicker upper layer and a faster current is expected (e.g., Chao, 1988; Lentz & Largier, 2006), where Lentz and Largier (2006) demonstrated that it is mainly moderate downwelling winds that increase the propagation speed and plume thickness. Our data suggest that this is also happening in our plume.

The arrival times of the fronts observed in Figure 6 seem to align with the work of de Boer et al. (2008). On a neap tide the fronts arrive around HW+2, which agrees with the timing of tidal straining and advection. During a spring tide the magnitude of advection increases, resulting in an earlier arrival (De Boer et al., 2006). When downwelling winds are added the entire alongshore flow is accelerated resulting in an even earlier arrival of the fronts. If we compare the arrival of the fronts with the frontal speed (U_f) no clear relation has been found (Figure 7). Fast arrival does not align always with a fast frontal propagation; some with the fastest arrival have a quite low frontal speed compared to the other fronts. Therefore, it seems that the fronts in this system are mainly advected by the tide and winds. Additionally, no clear evidence of downwelling velocities has been observed for the thick and fast fronts on spring tide with high downwelling winds. Therefore, advection and suppression of the lenses seems to be the explanation of the thick fronts under SW winds.

The radar images in Figures 4a and 4g show that the front is moving towards the coast and alongshore, where the alongshore component appears to be larger during spring tide with SW winds than during neap tide. In Figure A1 the alongshore movement of the front is highlighted using two red crosses that follow an irregularity on the front. The higher alongshore movement during spring tide with SW winds coincides with the

larger alongshore tidal currents and alongshore accelerated flow due to downwelling winds, respectively. The along-front velocity in the ambient flow and at the timing of the front confirms the presence of alongshore movement, which is larger for larger tidal amplitude and larger positive alongshore wind stress (not shown here). These results show that the intrinsic frontal speed could have an alongshore component, which is now neglected in our calculation, which could affect the magnitude and direction of U_f.

5.3. What is Driving Bottom Impact?

Peak bottom stresses are often observed at or near the time of frontal passage. However, the duration of elevated stress is often much longer than the time it takes for the front to pass and it is unclear whether the observed bed impacts are the result of processes localized at the front, or whether the front is associated with a change in the water column hydrodynamics that leads to increased bed stress. In other words, are the observed frontal impacts the result of strong tidal stresses modified by the rapidly changing stratification associated with frontal passage, or are their impacts associated with frontal processes themselves? Figures 4, 7, and 9 show that for periods with SW winds higher bed stresses are observed. Figure 4 shows clearly that the peak of the increasing bed stress happens after frontal arrival in the range of 0 to 30 min. For other periods, stresses close to the tidal stress seem to be observed. The extra observed peaks appear to be caused by other processes than the tide. Figure 10 will be used to investigate which mechanisms are causing the extra bed stress in the presence of strong stratification. Figure 10 shows the salinity difference, bed stress, dissipation and vertical velocity for the four selected periods in which a different response is observed. During the neap and spring period with low winds there is no extra signal of bed stress observed besides the tide.

The alignment of the peaks of front, bed stress and dissipation during the period SP-NP SW M (Figures 10m–10p) suggests elevated turbulence near the sea bed due to the arrival of the front. The dissipation values of 10^{-4} m^2 s^{-3} are in agreement with values found in the Columbia river plume (Orton & Jay, 2005). In addition, a sudden increase in the magnitude of downwelling velocities are observed around frontal passage, resulting in velocities in the order of −8 cm/s. These vertical velocities are smaller than values found in the Connecticut plume of −15 to −20 cm/s (O'Donnell et al., 1998) but larger than the values found in the Chesapeake Bay plume of −3 cm/s (Marmorino & Trump, 2000). Orton and Jay (2005) found downwelling velocities of −35 cm/s coinciding with strong near-bed velocities that were able to resuspend fine sediment in association with frontal passage during spring tide in the Columbia river plume.

The response near the seabed seems to be different during the spring period with high SW winds (Figures 10i–10l). A large peak in bed stress has been observed 30 min after frontal arrival, which is a large time frame to be ascribed only to frontal passage. The lack of a peak in dissipation during frontal arrival suggests that other processes are key in exerting the bed stress. Figures 7f–7h suggests that the alongshore wind stress accelerates the plume and lenses, resulting in a fast upper layer velocity and return flow below the front and lens. According to the classical theory the return current (u_2) below the upper layer accelerates relative to the (ambient) flow (u, see Figure 1), and it suggests that the return flow is larger for larger h. In our system, the return flow below the front acts at the same time and direction as cross-shore straining and advection. Therefore, the total acceleration of the return flow, due to frontal passage and straining, seems to be linked to the increase in bed stress. Because the system is so shallow the exchange flow at the coast due to fronts and straining can have a significant impact on sediment dynamics. Whether this mechanism operates in other systems is less clear for us.

6. Conclusion

This paper has presented that the leading edge of freshwater lenses in the Rhine river plume shows some basic frontal properties as observed in classical theory and other plume systems, such as a plunging head and the magnitude of frontal propagation speed. However, these Rhine plume fronts appear to behave quite differently as well, because of the mooring location and the 3-D tidal currents in a frictional system. A Froude number analysis suggested that the wind and tide mainly influence the fronts by advection instead of changing their structure. We observed differences in structure, thickness and arrival time between a calm neap and spring tide. Fast advection and thick fronts are observed under downwelling winds. In addition, peak bed stresses are observed at or near the timing of frontal passage under forcing of downwelling winds, coinciding with high near bed velocities. The bed impact seems to be the result of strong tidal stresses modified by the rapidly changing stratification associated with frontal passage; however, sometimes the impact seems to be associated with frontal processes itself.

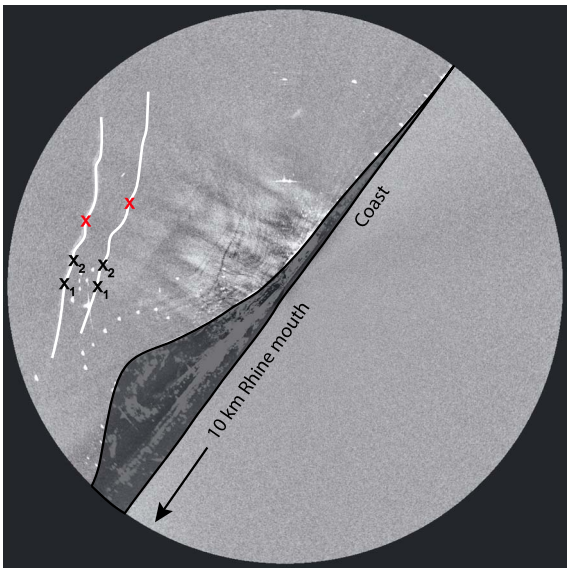

Figure A1. Front tracking system. Frontal speed is estimated by comparing radar images at two different times (white lines). Black crosses are used to estimate the frontal propagation speed and the red crosses indicate the alongshore movement. Image is of 17 September 2014, 09:42—09:57 (day 260).

Appendix A: Front Tracking Procedure

The X-band radar images in combination with the ADCP data are used to calculate frontal propagation speed U_f. This speed is defined as the speed relative to the ambient current normal to the front, $U_f = u_f - u_a$. The steps taken to derive U_f are explained below.

First, the radar images are used to estimate the frontal propagation speed relative to the ground (u_f) by following the front in time. More specific, a grid based on real-world coordinates is made for every radar image. Then the distance between two frontal lines, which are 20 min apart, is estimated. The speed relative to the ground (u_f) is determined using the expression $\Delta u = \Delta x/\Delta t$. For each image two points on the first and second frontal line close to the 12m mooring site are selected (Figure A1, x_1, and x_2). The estimated front normal velocity for both points are averaged.

Second, the ambient velocity u_a has been computed using the ADCP data 20 min (two bins) before frontal arrival averaged over the frontal/plume thickness. To be in a front-normal reference system, the ADCP data have been rotated into front-normal and along-front direction using the angle between the front and the coast. The information of the angle of the front has been extracted from the radar images.

Third, a quality check on the radar images has been performed, which resulted in 17 frontal occurrences that can be used. First, there are no images available of days 270.95 till 272.5 (27 September till 29 September). Then sometimes the fronts are too light or not even visible to determine an accurate angle and velocity. In addition, a few images were discarded because the propagation of the front and angle was difficult to determine. These fronts seemed to be arrested and quite unstable for a certain amount of time.

Additionally, some radar images showed very clearly the alongshore propagation of the fronts. Therefore, a third point has been marked on Figure A1 (red), which follows an irregularity on the front. The marker clearly shows the alongshore movement of the front. Not all images show a clear reference point to be able to calculate accurate along front velocities.

Acknowledgments
The authors would like to thank Ad Stolk, Rijkswaterstaat and the crew of the R.V. Zirfea. We also would like to thank Martijn Henriquez, Saulo Meirelles, Margaret McKeon, Richard Cooke, and Christopher Balfour for their valuable contribution during the STRAINS II measurement campaign (STRAtification Impacts Near-shore Sediment). We would like to thank Kevin Lamb for the nonhydrostatic model simulations (Lamb, 1994). The project is funded by the Netherlands Technology Foundation STW program project Sustainable engineering of coastal systems in Regions of Freshwater Influence (project 12682) and ERC-advanced grant 291206 Nearshore Monitoring and Modeling (NEMO). R. P. F. would like to thank the Fulbright Commission and CONICYT-Chile for the scholarship provided. ARH-D was supported by the Allan and Inger Osberg Professorship. A. J. S. was funded by NERC through NOC National Capability funding. Additionally, the authors are grateful for support provided by NERC to deploy the three bottom frames. The reviewers are thanked for their detailed comments, which substantially improved the manuscript. Tide and discharge data are obtained from the website of the Ministry of Infrastructure and Environment (the Hague, the Netherlands). Wind data are obtained from the Royal Netherlands Meteorological Institute (KNMI, de Bilt, the Netherlands). The data used in this paper are published as a data set in the 4TU Centre for Research Data in the Netherlands (Rijnsburger et al., 2018).

References

Benjamin, T. B. (1968). Gravity currents and related phenomena. *Journal of Fluid Mechanics*, *31*(2), 209–248.
Britter, R. E., & Simpson, J. E. (1978). Experiments on the dynamics of a gravity current head. *Journal of Fluid Mechanics*, *88*(2), 223–240.
Chao, S. (1988). Wind-driven motion of estuarine plumes. *Journal of Physical Oceanography*, *18*, 1144–1166.
Dagg, M., Benner, R., Lohrenz, S., & Lawrence, D. (2004). Transformation of dissolved and particulate materials on continental shelves influenced by large rivers: Plume processes. *Continental Shelf Research*, *24*(7–8), 833–858. https://doi.org/10.1016/j.csr.2004.02.003
De Boer, G. J., Pietrzak, J. D., & Winterwerp, J. C. (2006). On the vertical structure of the Rhine region of freshwater influence. *Ocean Dynamics*, *56*(3-4), 198–216. https://doi.org/10.1007/s10236-005-0042-1

de Boer, G. J., Pietrzak, J. D., & Winterwerp, J. C. (2007). SST observations of upwelling induced by tidal straining in the Rhine ROFI. *Continental Shelf Research*, *29*(1), 263–277. https://doi.org/10.1016/j.csr.2007.06.011

de Boer, G. J., Pietrzak, J. D., & Winterwerp, J. C. (2008). Using the potential energy anomaly equation to investigate tidal straining and advection of stratification in a region of freshwater influence. *Ocean Modelling*, *22*(1–2), 1–11. https://doi.org/10.1016/j.ocemod.2007.12.003

de Kok, J. (1996). A two-layer model of the Rhine plume. *Journal of Marine Systems*, *8*(3–4), 269–284. https://doi.org/10.1016/0924-7963(96)00010-3

de Kok, J. M. (1997). Baroclinic eddy formation in a Rhine plume model. *Journal of Marine Systems*, *12*(1–4), 35–52.

de Kok, J., de Valk, C., van Kester, J., de Goede, E., & Uittenbogaard, R. (2001). Salinity and temperature stratification in the Rhine plume. *Estuarine, Coastal and Shelf Science*, *53*(4), 467–475. https://doi.org/10.1006/ecss.2000.0627

de Ruijter, W. P. M., van der Giessen, A., & Groenendijk, F. C. (1992). Current and density structure in the Netherlands coastal zone. In D. Prandle (Ed.), *Dynamics and exchanges in estuaries and the coastal zone* (Vol. 40, pp. 529–550). Washington, DC: American Geophysical Union.

de Ruijter, W. P. M., Visser, A. W., & Bos, W. G. (1997). The Rhine outflow: A prototypical pulsed discharge plume in a high energy shallow sea. *Journal of Marine Systems*, *12*, 263–276.

Fischer, E., Burchard, H., & Hetland, R. D. (2009). Numerical investigations of the turbulent kinetic energy dissipation rate in the Rhine region of freshwater influence. *Ocean Dynamics*, *59*(5), 629–641.

Flores, R. P., Rijnsburger, S., Horner-Devine, A. R., Souza, A. J., & Pietrzak, J. D. (2017). The impact of storms and stratification on sediment transport in the Rhine region of freshwater influence. *Journal of Geophysical Research: Oceans*, *122*, 4456–4477. https://doi.org/10.1002/2016JC012362

Fong, D. A., & Geyer, W. R. (2001). Response of a river plume during an upwelling favorable wind event. *Journal of Geophysical Research*, *106*(C1), 1067–1084.

Garvine, R. W. (1974a). Physical features of the Connecticut River outflow during high discharge. *Journal of Geophysical Research*, *79*(6), 831–846.

Garvine, R. W. (1974b). Dynamics of small-scale oceanic fronts. https://doi.org/10.1175/1520-0485(1974)004<0557:DOSSOF>2.0.CO;2

Garvine, R. W., & Monk, J. D. (1974). Frontal structure of a river plume. *Journal of Geophysical Research*, *79*(15), 2251–2259.

Goring, D. G., & Nikora, V. I. (2002). Despiking acoustic Doppler velocimeter data. *Journal of Hydraulic Engineering*, *128*(1), 117–126.

Horner-Devine, A. R., Chickadel, C. C., & MacDonald, D. G. (2013). Coherent structures and mixing at a river plume front. In J. G. Venditti, J. L. Best, M. Church, & R. J. Hardy (Eds.), *Coherent flow structures at Earth's surface*. Chichester, UK: John Wiley.

Horner-Devine, A. R., Hetland, R. D., & MacDonald, D. G. (2015). Mixing and transport in coastal river plumes. *Annual Review of Fluid Mechanics*, *47*, 569–594. https://doi.org/10.1146/annurev-fluid-010313-141408

Horner-devine, A. R., Pietrzak, J. D., Souza, A. J., Mckeon, M. A., Meirelles, S., Henriquez, M., et al. (2017). Cross-shore transport of nearshore sediment by river plume frontal pumping. *Geophysical Research Letters*, *44*, 6343–6351. https://doi.org/10.1002/2017GL073378

Joordens, J. C. A., Souza, A. J., & Visser, A. (2001). The influence of tidal straining and wind on suspended matter and phytoplankton distribution in the Rhine outflow region. *Continental Shelf Research*, *21*, 301–325.

Kabat, P., Fresco, L. O., Stive, M. J. F., Veerman, C. P., van Alphen, J. S. L. J., Parmet, B. W. A. H., et al. (2009). Dutch coasts in transition. *Nature Geoscience*, *2*(7), 450–452. https://doi.org/10.1038/ngeo572

Kilcher, L. F., & Nash, J. D. (2010). Structure and dynamics of the Columbia River tidal plume front. *Journal of Geophysical Research*, *115*, C05S90. https://doi.org/10.1029/2009JC006066

Kourafalou, V. H., Oey, L.-Y., Wang, J. D., & Lee, T. N. (1996). The fate of river discharge on the continental shelf: 1. Modeling the river plume and the inner shelf coastal current. *Journal of Geophysical Research*, *101*(C2), 3415–3434.

Lamb, K. G. (1994). Lamb_JGR1994.pdf. *Journal of Geophysical Research*, *99*, 843–864.

Lentz, S. J., & Largier, J. (2006). The influence of wind forcing on the Chesapeake Bay buoyant coastal current. *Journal of Physical Oceanography*, *2005*, 1305–1316.

Luketina, D. A., & Imberger, J. (1987). Characteristics of a surface buoyant jet. *Journal of Geophysical Research*, *92*(C5), 5435–5447.

Marmorino, G. O., & Trump, C. L. (2000). Gravity current structure of the Chesapeake Bay outflow plume. *Journal of Geophysical Research*, *105*, 28,847–28,861.

Moffat, C., & Lentz, S. (2012). On the response of a buoyant plume to downwelling-favorable wind stress. *Journal of Physical Oceanography*, *42*, 1083–1098.

Nash, J. D., Kilcher, L. F., & Moum, J. N. (2009). Structure and composition of a strongly stratified, tidally pulsed river plume. *Journal of Geophysical Research*, *114*, C00B12. https://doi.org/10.1029/2008JC005036

Nash, J. D., & Moum, J. N. (2005). River plumes as a source of large-amplitude internal waves in the coastal ocean. *Nature*, *437*(7057), 400–403. https://doi.org/10.1038/nature03936

Nicholls, R. J., & Cazenave, A. (2010). Sea level rise and its impact on coastal zones. *Science*, *328*(2010), 1517–1520. https://doi.org/10.1126/science.1185782

O'Donnell, J. (1988). A numerical technique to incorporate frontal boundaries in two-dimensional layer models of ocean dynamics. *Journal of Physical Oceanography*, *18*, 1584–1600.

O'Donnell, J. (1990). The formation and fate of a river plume: A numerical model. *Journal of Physical Oceanography*, *20*(4), 551–569. https://doi.org/10.1175/1520-0485(1990)020<0551:TFAFOA>2.0.CO;2

O'Donnell, J., Marmorino, G. O., & Trump, C. L. (1998). Convergence and downwelling at a river plume front. *Journal of Physical Oceanography*, *28*, 1481–1495. https://doi.org/10.1175/1520-0485(1998)028<1481:CADAAR>2.0.CO;2

Orton, P. M., & Jay, D. A. (2005). Observations at the tidal plume front of a high-volume river outflow. *Geophysical Research Letters*, *32*, L11605. https://doi.org/10.1029/2005GL022372

Pawlowicz, R., Beardsley, B., & Lentz, S. (2002). Classical tidal harmonic analysis including werror estimates in MATLAB using T_TIDE. *Computers and Geosciences*, *28*(8), 929–937.

Rijkswaterstaat (2015). Watergegegevens. Retrieved from http://www.rijkswaterstaat.nl/water/waterdatawaterberichtgeving/watergegevens/

Rijnsburger, S., Flores, R. P., Pietrzak, J. D., Horner-Devine, A. R., Souza, A. J. (2018). Frontal periods. [Data Set]. Retrieved from https://doi.org/10.4121/uuid:5d0c5be2-8294-4e05-a859-7968cfd9bac1

Rijnsburger, S., van der Hout, C. M., van Tongeren, O., de Boer, G. J., van Prooijen, B. C., Borst, W. G., & Pietrzak, J. D. (2016). Simultaneous measurements of tidal straining and advection at two parallel transects far downstream in the Rhine ROFI. *Ocean Dynamics*, *66*(5), 719–736.

Shaw, W. J., & Trowbridge, J. H. (2001). The direct estimation of near-bottom turbulent fluxes in the presence of energetic wave motions. *Journal of Atmospheric and Oceanic Technology*, *18*(9), 1540–1557.

Shin, J. O., Dalziel, S. B., & Linden, P. F. (2004). Gravity currents produced by lock exchange. *Journal of Fluid Mechanics*, *521*, 1–34.

Simpson, J. H., & Souza, A. J. (1995). Semidiurnal switching of stratification in the region of the Rhine. *Journal of Geophysical research*, *100*, 7037–7044.

Souza, A. J., & Simpson, J. H. (1996). The modification of tidal ellipses by stratification in the Rhine ROFI. *Continental Shelf Research*, *16*(8), 997–1007.

Spahn, E. Y., Horner-Devine, A. R., Nash, J. D., Jay, D. A., & Kilcher, L. (2009). Particle resuspension in the Columbia River plume near field. *Journal of Geophysical Research*, *114*, C00B14. https://doi.org/10.1029/2008JC004986

Stive, M. J. F., de Schipper, M. A., Luijendijk, A. P., Aarninkhof, S. G., van Gelder-Maas, C., de Vries, J. S. V. T., et al. (2013). A new alternative to saving our beaches from sea-level rise: The Sand Engine. *Journal of Coastal Research*, *29*(5), 1001–1008.

Van Alphen, J. S. L. J., De Ruijter, W. P. M., & Borst, J. C. (1988). Outflow and three-dimensional spreading of Rhine river water in the Netherlands coastal zone. In J. Dronkers & W. van Leussen (Eds.), *Physical processes in estuaries* (pp. 70–92). Berlin: Springer-Verlag.

Visser, A. W., Souza, A. J., Hessner, K., & Simpson, J. H. (1994). The effect of stratification on tidal current profiles in a region of freshwater influence. *Oceanologica Acta*, *17*(4), 369–381.

Voulgaris, G., & Trowbridge, J. H. (1998). Evaluation of the acoustic Doppler velocimeter (ADV) for turbulence measurements *. *Journal of Atmospheric and Oceanic Technology*, *15*, 272–289.

Yankovsky, A. E., & Chapman, D. C. (1997). A simple theory for the fate of buoyant coastal discharges*. *Journal of Physical Oceanography*, *27*(7), 1386–1401.